

Geometric Backstepping Control of Omnidirectional Tiltrotors Incorporating Servo–Rotor Dynamics for Robustness against Sudden Disturbances

Jaewoo Lee^{1*}, Dongjae Lee^{2*}, Jinwoo Lee¹, Hyungyu Lee³, Yeonjoon Kim¹, and H. Jin Kim¹

Abstract—This work presents a geometric backstepping controller for a variable-tilt omnidirectional multirotor that explicitly accounts for both servo and rotor dynamics. Considering actuator dynamics is essential for more effective and reliable operation, particularly during aggressive flight maneuvers or recovery from sudden disturbances. While prior studies have investigated actuator-aware control for conventional and fixed-tilt multirotors, these approaches rely on linear relationships between actuator input and wrench, which cannot capture the nonlinearities induced by variable tilt angles. In this work, we exploit the cascade structure between the rigid-body dynamics of the multirotor and its nonlinear actuator dynamics to design the proposed backstepping controller and establish exponential stability of the overall system. Furthermore, we reveal parametric uncertainty in the actuator model through experiments, and we demonstrate that the proposed controller remains robust against such uncertainty. The controller was compared against a baseline that does not account for actuator dynamics across three experimental scenarios: fast translational tracking, rapid rotational tracking, and recovery from sudden disturbance. The proposed method consistently achieved better tracking performance, and notably, while the baseline diverged and crashed during the fastest translational trajectory tracking and the recovery experiment, the proposed controller maintained stability and successfully completed the tasks, thereby demonstrating its effectiveness.

I. INTRODUCTION

Fully actuated multirotors have attracted growing attention as a powerful means to overcome the inherent underactuation of conventional multirotor platforms [1]. Owing to their full actuation capability, these platforms can generate horizontal forces and achieve translational motion without tilting their roll and pitch angles. Such characteristics enable a variety of applications, including the transportation of payloads without attitude changes [2], physical interaction with the environment [3], and aerial manipulation tasks [4].

Building on these advances, omnidirectional multirotors have been developed to further equip with the hovering

*The first two authors contributed equally to this work.

¹Department of Aerospace Engineering, Seoul National University (SNU), Seoul 08826, South Korea {jaewoolee930, jinwoolee0728, 0831joon, hjinkim}@snu.ac.kr

²Robotics Institute, Carnegie Mellon University, Pittsburgh, PA 15217, USA dongjae2@andrew.cmu.edu

³Department of Mechanical Science and Engineering, University of Illinois Urbana-Champaign, Champaign, IL 61801, USA hyungyu2@illinois.edu

This work was supported by the National Research Foundation of Korea(NRF) grant funded by the Korea government(MSIT)(RS-2024-00436984). Dongjae Lee was supported by Basic Science Research Program through the National Research Foundation of Korea(NRF) funded by the Ministry of Education(RS-2025-02634317).

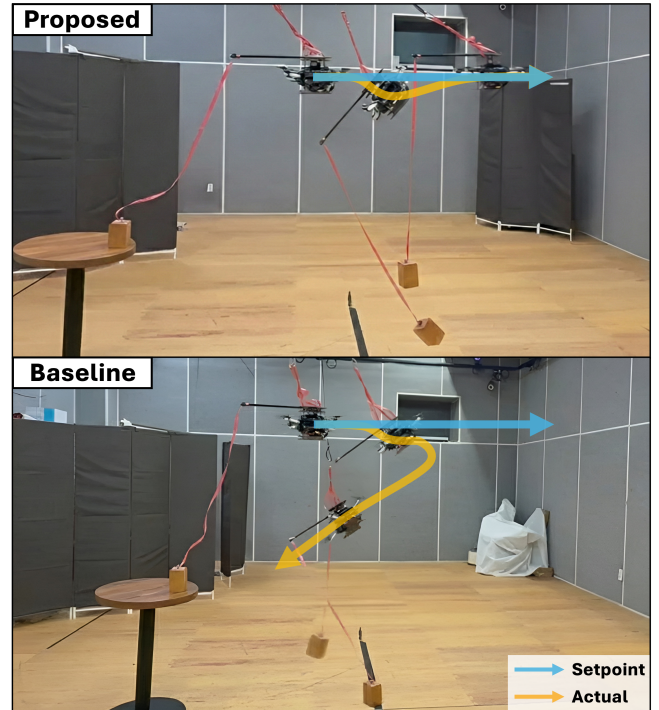


Fig. 1. Time-lapse composite images from the experiments. Blue arrows indicate the commanded setpoint direction, and yellow arrows trace the actual trajectory. A sudden disturbance is induced by a falling object connected to the omnidirectional multirotor via a red cable. The proposed controller (Top) successfully stabilizes the vehicle and follows the setpoint, whereas the baseline (Bottom) diverges and crashes.

capability in arbitrary orientations [5]–[7]. Their capability to hover at arbitrary orientations, referred to as omnidirectionality in attitude, has attracted considerable attention for tasks such as contact-based inspection of curved surfaces [8] and expanding the workspace of aerial manipulation systems [9]. These capabilities highlight the growing potential of omnidirectional multirotors in complex real-world operations.

To fully exploit the advantages of omnidirectional flight and to ensure reliable operation, it is essential to incorporate *actuator dynamics*, the dynamics of rotors and servos, into the control design. Many prior studies, however, have relied on control allocation methods that compute the desired actuator input from the desired wrench and then directly treat this value as the actual actuator input [6], [8]–[10]. Such an approach implicitly assumes that actuators can instantaneously realize any commanded input. This assumption may hold in slow or moderate maneuvers, but it becomes a critical issue when

the control input must change rapidly, as in agile trajectory tracking or in recovering from sudden external disturbances. In these scenarios, ignoring actuator dynamics can degrade control performance or even lead to flight instability and crashes as shown in Fig. 1 baseline.

To address these challenges, this work proposes a control strategy for omnidirectional variable-tilt multirotors that explicitly accounts for both rotor and servo dynamics, in contrast to previous studies that ignored actuator dynamics or considered only a single component such as the servo or rotor [7], [11]–[14]. We propose a geometric backstepping controller motivated by the cascaded structure between the rigid-body dynamics and the actuator dynamics.

We first design a wrench controller for the rigid-body dynamics without considering the actuator dynamics and derive an actuator controller in a backstepping manner [15] that takes into account the gap between the desired wrench command and the actual wrench. Moreover, unlike prior studies that considered actuator dynamics only at the control allocation level and either locally linearized or entirely omitted their influence on the overall system dynamics [12], [16], we conduct a Lyapunov-based stability analysis of the full closed-loop system that explicitly incorporates actuator dynamics. Through the analysis, we show that the entire system is exponentially stable. Finally, we further show that the proposed controller is also robust to parametric uncertainties in the time constant terms inherent to actuator dynamics.

The main contributions of this paper are summarized as follows:

- A geometric backstepping control framework for variable-tilt omnidirectional multirotors that explicitly incorporates the first-order dynamics of both servos and motors.
- A rigorous stability analysis of the full closed-loop system, establishing exponential stability for known actuator time constants and ultimate boundedness under uncertainty in these parameters.
- Validation of the proposed controller through real-world experiments, including high-speed trajectory tracking and recovery from impulsive rotational disturbances. The results demonstrate that our method significantly outperforms a baseline controller, which fails to maintain stability during aggressive maneuvers.

II. RELATED WORK

Many existing control strategies for conventional multirotors [17], [18] and omnidirectional multirotors [6], [8]–[10] simplify the problem by assuming that actuators can respond instantaneously to commanded inputs. While effective for slow movements, this assumption fails during fast trajectory tracking or when recovering from external disturbances.

To address this issue, recent works begin to incorporate actuator dynamics directly into the controller design. For conventional multirotors, incorporating first-order rotor dynamics improves high speed tracking and robustness [19], [20]. For fixed-tilt platforms where servo dynamics are absent,

research has focused on the impact of rotor dynamics. Some studies have modeled the rotor angular speed dynamics as a first-order system and implemented an angular velocity feedback controller [21]. Similarly, a geometric tracking controller was proposed that incorporated a first-order wrench dynamics model [22]. However, for variable-tilt platforms, the wrench dynamics cannot be represented by a single first-order system due to the nonlinearity of the control allocation map. Consequently, variable-tilt multirotors require control strategies that explicitly accommodate these additional nonlinearities.

Another challenge for variable-tilt platforms is the slower response of the tilt servos. To address this problem, a Smith predictor was employed to compensate for known servo delays [7]. A quasi-decoupling controller was also developed, which uses the current servo angle for control allocation to achieve performance independent of the servo’s response time [23]. A similar approach to using the current servo angle in control allocation was also devised in [13] from the observation of slower servomotor response than the rotor response. A common limitation of these approaches is their focus on either rotor or servo dynamics in isolation.

More recently, efforts have been made to address both actuator dynamics simultaneously. For instance, an approach using Nonlinear Model Predictive Control (NMPC) modeled both rotor thrust dynamics and servo angle dynamics as first-order systems [11]. However, the substantial computational burden of NMPC remains particularly challenging in scenarios that require high-frequency control and rapid, large changes in actuator inputs. A different strategy, known as differential allocation, addresses actuator velocity limits and dynamics directly within the control allocation module [12]. This approach was later extended to incorporate the power dynamics of the actuators, providing a more comprehensive model at the allocation level [16]. However, while these methods are effective, their focus remains on solving the allocation problem itself. Consequently, they do not provide a formal stability analysis for the entire closed-loop system, where the vehicle’s rigid-body dynamics are fully coupled with the actuator dynamics, and stability claims in these works are confined to simplified or linearized models. Furthermore, they rely on the assumption of a perfectly known model and do not provide a robustness analysis against model uncertainties.

III. CONTROLLER DESIGN

A. Notations

In this section, we define the key notations used throughout this work. For vectors $a, b \in \mathbb{R}^3$, the hat map is defined as $\hat{a}b = a \times b$, which maps a vector to a skew-symmetric matrix. The symbol $(\cdot)^\vee$ denotes its inverse transformation. $\text{tr}(\cdot)$ denotes the trace of a matrix, and $\text{sat}_\sigma(y)$ is defined as $\sigma \cdot \text{sign}(y)$ if $|y| > \sigma$, and y otherwise.

$\|\cdot\|$ represents the 2-norm when applied to a vector and the induced 2-norm when applied to a matrix. $\|a\|_\infty$ denotes the infinity norm of a vector a . The notation $\|\cdot\|_F$ represents

the Frobenius norm of a matrix, which is defined as:

$$\|A\|_F = \sqrt{\sum_{i,j} |A_{ij}|^2}. \quad (1)$$

For a square matrix A , the maximum and minimum eigenvalues are denoted by $\lambda_{\max}(A)$ and $\lambda_{\min}(A)$, respectively. The notation B^\dagger denotes the pseudo-inverse of a non-square matrix B . The notation $\text{blockdiag}(A_1, A_2, \dots, A_k)$ denotes a block-diagonal matrix with blocks A_1, A_2, \dots, A_k on the diagonal. $[a; b]$ represents the concatenation of two column vectors a and b , which is defined as $[a; b] := [a^\top, b^\top]^\top$. The $n \times n$ identity matrix is denoted as I_n .

B. System Dynamics

We consider the variable-tilt multirotor as in [6], [7], [10]. The total thrust f and torque τ are expressed as a combination of rotor thrusts and servo angles:

$$\begin{aligned} f &= \sum_{i=1}^n {}^B R_i f_i \\ \tau &= \sum_{i=1}^n [l_i \times {}^B R_i f_i \pm k_f {}^B R_i f_i] \end{aligned} \quad (2)$$

where $n > 3$ is the number of rotors, ${}^B R_i \in SO(3)$ is the corresponding rotation matrix of the i^{th} servo angle expressed in the multirotor body frame, $f_i \in \mathbb{R}$ is the i^{th} rotor thrust, and $l_i \in \mathbb{R}^3$ and $k_f \in \mathbb{R}$ are the displacement vectors of the i^{th} rotor from the geometric center of the multirotor and the aerodynamic drag coefficient of the rotors. Using f and τ defined in (2), the equations of motion of the omnidirectional tiltrotor, including the dynamics of the rotors and servo motors, are given as follows:

$$\begin{aligned} \ddot{p} &= \frac{1}{m} R f - g e_3 + \Delta_p \\ \dot{R} &= R \hat{\omega} \end{aligned} \quad (3a)$$

$$\begin{aligned} \dot{\omega} &= J^{-1}(-\omega \times J \omega + \tau) + \Delta_R \\ \dot{f}_i &= \frac{1}{\alpha_f} (f_{c_i} - f_i) \\ \dot{\theta}_i &= \frac{1}{\alpha_\theta} (\theta_{c_i} - \theta_i) \end{aligned} \quad (3b)$$

where $p, \omega \in \mathbb{R}^3$ and $R \in SO(3)$ are the position, body angular velocity, and the orientation of the multirotor. i^{th} rotor thrust and servomotor angle are f_i and θ_i , respectively. $m, g \in \mathbb{R}$ are mass of the multirotor and the gravitational acceleration constant, $J \in \mathbb{R}^{3 \times 3}$ is the mass moment of inertia of the multirotor, and $\alpha_f, \alpha_\theta \in \mathbb{R}$ are the actuator time constants. We model the thrust directly as a first-order system to bypass the nonlinearity of the rotor speed-to-thrust mapping, a choice that balances modeling accuracy with controller simplicity, as discussed in [22]. $\Delta_p, \Delta_R \in \mathbb{R}^3$ are constant translational and rotational disturbance. Lastly, $f_{c_i}, \theta_{c_i} \in \mathbb{R}$ are the rotor thrust and servo angle commands.

For the ease of controller design, we define the vector $u \in \mathbb{R}^{2n}$ as

$$u = [f_1 \cos \theta_1, f_1 \sin \theta_1, f_2 \cos \theta_2, f_2 \sin \theta_2, \dots, f_n \sin \theta_n]^\top.$$

Accordingly, the resulting total wrench is computed as

$$\mu := \begin{bmatrix} f \\ \tau \end{bmatrix} = B u \quad (4)$$

where $B \in \mathbb{R}^{6 \times 2n}$ denotes the allocation matrix [6]. Then, the rigid-body dynamics (3a) can be reformulated as

$$\begin{bmatrix} \ddot{p} \\ \dot{\omega} \end{bmatrix} = \begin{bmatrix} -g e_3 \\ J^{-1}(-\omega \times J \omega) \end{bmatrix} + \begin{bmatrix} \frac{1}{m} R & 0 \\ 0 & J^{-1} \end{bmatrix} \mu + \begin{bmatrix} \Delta_p \\ \Delta_R \end{bmatrix}. \quad (5)$$

The actual control input, denoted by u_c , is defined as follows:

$$u_c = [f_{c_1}, \theta_{c_1}, f_{c_2}, \theta_{c_2}, \dots, f_{c_n}, \theta_{c_n}]^\top$$

To characterize \dot{u} , we examine the time derivatives of its first two components:

$$\begin{aligned} \begin{bmatrix} \dot{u}_1 \\ \dot{u}_2 \end{bmatrix} &= \begin{bmatrix} \dot{f}_1 \cos \theta_1 - f_1 \sin \theta_1 \dot{\theta}_1 \\ \dot{f}_1 \sin \theta_1 + f_1 \cos \theta_1 \dot{\theta}_1 \end{bmatrix} \\ &= \begin{bmatrix} -\frac{u_1}{\alpha_f} + \frac{u_2}{\alpha_\theta} \tan^{-1} \frac{u_2}{u_1} \\ -\frac{u_2}{\alpha_f} - \frac{u_1}{\alpha_\theta} \tan^{-1} \frac{u_2}{u_1} \end{bmatrix} + \begin{bmatrix} \frac{1}{\alpha_f} \frac{u_1}{\sqrt{u_1^2 + u_2^2}} & -\frac{u_2}{\alpha_\theta} \\ \frac{1}{\alpha_f} \frac{u_2}{\sqrt{u_1^2 + u_2^2}} & \frac{u_1}{\alpha_\theta} \end{bmatrix} \begin{bmatrix} f_{c_1} \\ \theta_{c_1} \end{bmatrix} \\ &=: \zeta_1(u) + \eta_1(u) \begin{bmatrix} f_{c_1} \\ \theta_{c_1} \end{bmatrix} \end{aligned}$$

Generalizing the above result to all columns, \dot{u} can be written as follows:

$$\dot{u} = \zeta(u) + \eta(u) u_c \quad (6)$$

where $\zeta(u) := [\zeta_1; \zeta_2; \dots; \zeta_n] \in \mathbb{R}^{2n}$, $\eta(u) := \text{blockdiag}(\eta_1, \eta_2, \dots, \eta_n) \in \mathbb{R}^{2n \times 2n}$. To avoid ill-posedness of (6), we assume that $f_i \neq 0 \forall i$.

C. Backstepping Controller Design

Observing the structures of (3a) and (3b), once f_{c_i} and θ_{c_i} are determined, f and θ are computed from the actuator dynamics, which then define the rigid-body dynamics. This forms a cascaded structure. Inspired by [15], we exploit this cascaded structural property to design a backstepping controller and ensure the stability of the overall system. The proposed backstepping controller is organized as follows: first, a nominal controller for the desired control input μ_d is constructed by considering only the rigid-body dynamics while neglecting the actuator dynamics. Next, using the difference between the desired control input μ_d and the actual control input μ , defined as $e_\mu = \mu - \mu_d$, a candidate Lyapunov function is formulated. By analyzing this function, we derive the final actuator-level control input u_c that guarantees system stability.

Let us first revisit $Bu = \mu = \mu_d + e_\mu$ where $e_\mu = \mu - \mu_d$, and let $\mu_d = [\mu_{d,1}; \mu_{d,2}]$, $e_\mu = [e_{\mu,1}; e_{\mu,2}]$ where $\mu_1, \mu_2, e_{\mu,1}, e_{\mu,2} \in \mathbb{R}^3$. Errors in position e_p , linear velocity e_v , rotation e_R , and angular velocity e_ω are defined as follows:

$$\begin{aligned} e_p &= p - p_d, & e_v &= v - v_d, \\ e_R &= \frac{1}{2} (R_d^\top R - R^\top R_d)^\vee, & e_\omega &= \omega - R^\top R_d \omega_d \end{aligned} \quad (7)$$

Then, the error dynamics for the rigid-body dynamics (5) can be computed as follows:

$$\begin{bmatrix} \dot{e}_v \\ \dot{e}_\omega \end{bmatrix} = F + G(\mu_d + e_\mu) + \Delta \quad (8)$$

where

$$F = \begin{bmatrix} -ge_3 - \dot{v}_d \\ J^{-1}(-\omega \times J\omega) + \hat{\omega}R^\top R_d \omega_d - R^\top R_d \dot{\omega}_d \end{bmatrix},$$

$$G = \begin{bmatrix} \frac{1}{m}R & 0 \\ 0 & J^{-1} \end{bmatrix}, \quad \Delta = \begin{bmatrix} \Delta_p \\ \Delta_R \end{bmatrix}.$$

Define μ_d using [24] as the following, which guarantees exponential stability if $e_\mu = 0$:

$$\begin{aligned} \mu_{d,1} &= mR^\top (-k_{tp}e_p - k_{td}e_v - k_{ti}\text{sat}_{\sigma_1}(e_{pi}) + ge_3 + \dot{v}_d) \\ \mu_{d,2} &= \omega \times J\omega - J(\hat{\omega}R^\top R_d \omega_d - R^\top R_d \dot{\omega}_d) - k_{rp}e_R \\ &\quad - k_{rd}e_\omega - k_{ri}\text{sat}_{\sigma_2}(e_{ri}) \end{aligned} \quad (9)$$

where, $k_{tp}, k_{td}, k_{rp}, k_{rd}, k_{ti}, k_{ri}$ are positive constants. For positive constants c_1 and c_2 , e_{pi} and e_{ri} are defined as

$$e_{pi} = \int_0^t e_v(\tau) + c_1 e_p(\tau) d\tau, \quad e_{ri} = \int_0^t e_\omega(\tau) + c_2 e_R(\tau) d\tau. \quad (10)$$

Next, consider the candidate Lyapunov functions for the translational and rotational dynamics as

$$\begin{aligned} V_1 &:= \frac{1}{2}k_{tp}\|e_p\|^2 + \frac{1}{2}\|e_v\|^2 + c_1 e_p^\top e_v \\ &\quad + \int_{\frac{\Delta_p}{k_{pi}}}^{e_{pi}} (k_{pi}\text{sat}_{\sigma_1}(\gamma) - \Delta_p) \cdot d\gamma, \end{aligned} \quad (11)$$

$$\begin{aligned} V_2 &:= \frac{1}{2}e_\omega^\top J e_\omega + k_{rp}\Psi(R, R_d) + c_2 e_R^\top e_\omega \\ &\quad + \int_{\frac{\Delta_R}{k_{ri}}}^{e_{ri}} (k_{ri}\text{sat}_{\sigma_2}(\gamma) - \Delta_R) \cdot d\gamma, \end{aligned} \quad (12)$$

where $\Psi(R, R_d) = \frac{1}{2} \text{tr}(I - R_d^\top R)$. Positive-definiteness of the two candidate functions can be easily satisfied by defining $k_{pi}\sigma_1 > \|\Delta_p\|_\infty$ and $k_{ri}\sigma_2 > \|\Delta_R\|_\infty$ [24]. Unlike [24] where no actuator dynamics is considered, there exists the difference e_μ in the system dynamics (8) which interrupts exponential stability guarantee. To simultaneously account for the influence of e_μ on the system dynamics, we propose an augmented candidate Lyapunov function V as

$$V = \frac{1}{2}e_\mu^\top e_\mu + V_1 + V_2 \quad (13)$$

whose derivative is then used to obtain the final actuator control input u_c . We define u_c as follows:

$$u_c = \eta^{-1}B^\dagger(\dot{\mu}_d - B\zeta - k_\mu e_\mu - \kappa) \quad (14)$$

where $k_\mu > 0$ is a control parameter and

$$\kappa = \begin{bmatrix} \frac{c_1}{m}R^\top e_p + \frac{1}{m}R^\top e_v \\ c_2 J^{-1}e_R + e_\omega \end{bmatrix}. \quad (15)$$

ζ, η can be found from (6) and B appears in (4).

IV. STABILITY & ROBUSTNESS ANALYSIS

In the preceding section, a controller was designed using the backstepping approach. This section establishes exponential stability when the actuator time constant is known, and then demonstrates ultimate boundedness when the constant is unknown but its bound is available. Before these analyses, the conditions on the control gains and a lemma commonly used in both cases are presented.

Condition. For the constant parameters c_1, c_2 appearing in (10), (11), (12) and (15) and $k_{pi}, k_{ri}, \sigma_1, \sigma_2$ appearing in (11) and (12), we impose the following conditions:

$$c_1 < \min(\sqrt{k_{tp}}, \frac{4k_{tp}k_{td}}{k_{td}^2 + 4k_{tp}})$$

$$c_2 < \min(\sqrt{k_{rp}\lambda_{\min}(J)}, \frac{4\lambda_{\min}^2(J)k_{rp}k_{rd}}{4k_{rp}\lambda_{\min}^2(J) + k_{rd}^2\lambda_{\max}(J)})$$

$$k_{pi}\sigma_1 > \|\Delta_p\|_\infty, \quad k_{ri}\sigma_2 > \|\Delta_R\|_\infty. \quad (16)$$

Lemma 1. Assume that (16) holds. Then, for $z_1 = [\|e_p\|; \|e_v\|]$ and $z_2 = [\|e_R\|; \|e_\omega\|]$, the candidate Lyapunov function V is bounded by the following:

$$\begin{aligned} \frac{1}{2}e_\mu^\top e_\mu + z_1^\top M_{11}z_1 + z_2^\top M_{21}z_2 + V_I &\leq V \leq \\ \frac{1}{2}e_\mu^\top e_\mu + z_1^\top M_{12}z_1 + z_2^\top M_{22}z_2 + V_I, \end{aligned} \quad (17)$$

where $M_{11}, M_{12}, M_{21}, M_{22}$ are positive definite matrices and V_I is positive definite.

Proof. From [24], V_1 and V_2 are bounded by

$$\begin{aligned} z_1^\top M_{11}z_1 + V_{Ip} &\leq V_1 \leq z_1^\top M_{12}z_1 + V_{Ip} \\ z_2^\top M_{21}z_2 + V_{IR} &\leq V_2 \leq z_2^\top M_{22}z_2 + V_{IR} \end{aligned}$$

where the matrices $M_{11}, M_{12}, M_{21}, M_{22}$ are given by

$$\begin{aligned} M_{11} &= \frac{1}{2} \begin{bmatrix} k_{tp} & -c_1 \\ -c_1 & 1 \end{bmatrix}, \quad M_{12} = \frac{1}{2} \begin{bmatrix} k_{tp} & c_1 \\ c_1 & 1 \end{bmatrix} \\ M_{21} &= \frac{1}{2} \begin{bmatrix} k_{rp} & -c_2 \\ -c_2 & \lambda_{\min}(J) \end{bmatrix}, \quad M_{22} = \frac{1}{2} \begin{bmatrix} \frac{2k_{rp}}{2-\psi_2} & c_2 \\ c_2 & \lambda_{\max}(J) \end{bmatrix}, \end{aligned}$$

and V_{Ip} and V_{IR} are defined as

$$\begin{aligned} V_{Ip} &= \int_{\frac{\Delta_p}{k_{pi}}}^{e_{pi}} (k_{pi}\text{sat}_{\sigma_1}(\gamma) - \Delta_p) \cdot d\gamma \\ V_{IR} &= \int_{\frac{\Delta_R}{k_{ri}}}^{e_{ri}} (k_{ri}\text{sat}_{\sigma_2}(\gamma) - \Delta_R) \cdot d\gamma. \end{aligned}$$

From (16), $M_{11}, M_{12}, M_{21}, M_{22}$ are all positive-definite [24] and $V_{Ip} > 0$ and $V_{IR} > 0$ unless $k_{pi}e_{pi} = \Delta_p$ and $k_{ri}e_{ri} = \Delta_R$. Defining $V_I := V_{Ip} + V_{IR}$, this completes the proof. \square

A. Exponential stability analysis with known actuator dynamics

Theorem 1. Assume that conditions (16) hold and that parameters α_f, α_θ in (3b) are known. Then, the closed-loop system composed of (5), (6) and (14) is exponentially stable.

Proof. From the definitions of V_1 and V_2 in (11) and (12), we compute the time derivatives of V_1 and V_2 using the system dynamics (5) and the desired control input (9) as follows:

$$\begin{aligned} \dot{V}_1 &\leq e_{\mu,1}^\top (\frac{c_1}{m}R^\top e_p + \frac{1}{m}R^\top e_v) - z_1^\top W_1 z_1 \\ \dot{V}_2 &\leq e_{\mu,2}^\top (c_2 J^{-1}e_R + e_\omega) - z_2^\top W_2 z_2 \end{aligned} \quad (18)$$

where the matrices W_1 and W_2 are given by

$$W_1 = \frac{1}{2} \begin{bmatrix} c_1 k_{tp} & -\frac{1}{2}c_1 k_{td} \\ -\frac{1}{2}c_1 k_{td} & k_{td} - c_1 \end{bmatrix}, \quad W_2 = \frac{1}{2} \begin{bmatrix} \frac{c_2 k_{rp}}{\lambda_{\max}(J)} & -\frac{c_2 k_{rd}}{2\lambda_{\min}(J)} \\ -\frac{c_2 k_{rd}}{2\lambda_{\min}(J)} & k_{rd} - c_2 \end{bmatrix},$$

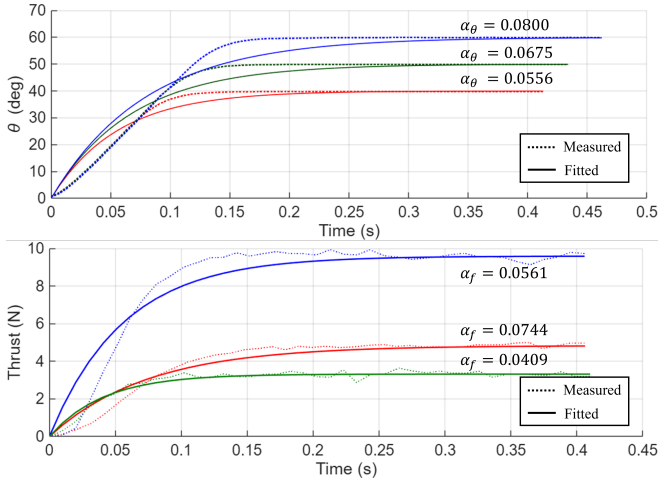


Fig. 2. Step responses of the rotor and servo to step commands of varying amplitude. The actuator time constant varies with step size, highlighting the need for robustness to uncertainty in this parameter.

and W_1, W_2 are positive definite by (16) [24].

From the definition of κ in (15), the definition of $e_\mu = \mu - \mu_d = Bu - \mu_d$, the actuator dynamics (6), (18), and the actuator control input u_c (14),

$$\begin{aligned} \dot{V} &\leq e_\mu^\top (Bu - \mu_d + \kappa) - z_1^\top W_1 z_1 - z_2^\top W_2 z_2 \\ &= e_\mu^\top (B(\zeta + \eta u_c) - \mu_d + \kappa) - z_1^\top W_1 z_1 - z_2^\top W_2 z_2 \quad (19) \\ &= -k_\mu e_\mu^\top e_\mu - z_1^\top W_1 z_1 - z_2^\top W_2 z_2 \end{aligned}$$

where we used the fact that $BB^\dagger = I_6$. At the equilibrium point with $k_{pi}e_{pi} = \Delta_p$ and $k_{ri}e_{ri} = \Delta_R$, since the Lyapunov function V is quadratically bounded by $[e_\mu; z_1; z_2]$ from Lemma 1 and its time-derivative is quadratically bounded by (19), the system is exponentially stable [24]. \square

B. Robustness analysis with uncertain actuator dynamics

Real hardware deviates from an ideal first-order actuator model, so uncertainty in actuator dynamics must be taken into account. To substantiate this, we experimentally measured the step responses of the actuators. As shown in Fig. 2, the identified time constants vary with the command setpoint, and a single first-order fit leaves noticeable residuals – up to 30% for the servo and up to 45% for the rotor. We therefore model the actuator dynamics with bounded uncertainty and analyze the controller accordingly. Crucially, guaranteeing stability under such uncertainty removes the need to identify an exact time constant for every actuator.

In this subsection, we establish the boundedness of the state error under the proposed controller in the presence of uncertainties in both the tiltrotor rigid-body dynamics and the actuator dynamics. To model actuator uncertainty, we treat the rotor and servo time constants to be unknown but bounded deviations around nominal values:

$$\alpha_f \in [\bar{\alpha}_f - \delta_f, \bar{\alpha}_f + \delta_f], \quad \alpha_\theta \in [\bar{\alpha}_\theta - \delta_\theta, \bar{\alpha}_\theta + \delta_\theta].$$

Lemma 2. For $x = [z_1; z_2; e_\mu]$, assume that $x \in \Omega_c = \{x | V(x) \leq c\}$ for a positive constant c . Furthermore, assume

that $\|\dot{v}_d\| \leq a_v$, $\|\omega_d\| \leq a_\omega$, $\|\dot{\omega}_d\| \leq a_{\dot{\omega}}$, and $\alpha_f \in [\bar{\alpha}_f - \delta_f, \bar{\alpha}_f + \delta_f]$, $\alpha_\theta \in [\bar{\alpha}_\theta - \delta_\theta, \bar{\alpha}_\theta + \delta_\theta]$. Then, the norms of $\Delta\zeta := \zeta - \bar{\zeta}$ and $\Delta\eta := \eta - \bar{\eta}$ are bounded by a positive constant.

Proof. From (17) and the assumption that $V(x) \leq c$,

$$\frac{1}{2} e_\mu^\top e_\mu + z_1^\top M_{11} z_1 + z_2^\top M_{21} z_2 + V_f \leq V \leq c. \quad (20)$$

Since all terms on the left-hand side are positive, e_μ, z_1, z_2 are bounded as follows:

$$\|e_\mu\| \leq \sqrt{2c}, \quad \|z_1\| \leq \sqrt{\frac{c}{\lambda_{\min}(M_{11})}}, \quad \|z_2\| \leq \sqrt{\frac{c}{\lambda_{\min}(M_{21})}}. \quad (21)$$

Substituting this condition into (9), we get

$$\|\mu_d\| \leq L_1 \|z_1\| + L_2 \|z_2\| + L_0 \quad (22)$$

where

$$\begin{aligned} L_1 &= m \sqrt{k_{rp}^2 + k_{td}^2} \\ L_2 &= \sqrt{k_{rp}^2 + (\lambda_{\max}(J) \sqrt{\frac{c}{\lambda_{\min}(M_{21})}} + 3a_w \lambda_{\max}(J) + k_{rd})^2} \\ L_0 &= m(g + a_v + k_{ti} \sigma_1) + \lambda_{\max}(J)(2a_w^2 + a_{\dot{w}}) + k_{ri} \sigma_2. \end{aligned} \quad (23)$$

From the equation $Bu = \mu_d + e_\mu$, applying (21) and (22), we obtain:

$$\begin{aligned} \|u\| &\leq \|B^\dagger\| \left\{ \sqrt{2c} + L_1 \sqrt{\frac{c}{\lambda_{\min}(M_{11})}} + L_2 \sqrt{\frac{c}{\lambda_{\min}(M_{21})}} + L_0 \right\} \\ &=: \rho(c). \end{aligned} \quad (24)$$

Since $\|u\| = \sqrt{\sum_{i=1}^n f_i^2} \leq \rho(c)$, it follows that

$$f_{\max} := \max_i f_i \leq \rho(c). \quad (25)$$

Using the initial assumption that α_f and α_θ are bounded around their nominal values, we define d_f and d_θ as follows:

$$\begin{aligned} \left| \frac{1}{\bar{\alpha}_f} - \frac{1}{\alpha_f} \right| &\leq \frac{\delta_f}{\bar{\alpha}_f(\bar{\alpha}_f - \delta_f)} =: d_f, \\ \left| \frac{1}{\bar{\alpha}_\theta} - \frac{1}{\alpha_\theta} \right| &\leq \frac{\delta_\theta}{\bar{\alpha}_\theta(\bar{\alpha}_\theta - \delta_\theta)} =: d_\theta. \end{aligned}$$

Using d_f and d_θ , $\Delta\zeta_i$ and $\Delta\eta_i$ can be expressed as follows:

$$\Delta\zeta_i = f_i \begin{bmatrix} d_f \cos \theta_i - d_\theta \theta_i \sin \theta_i \\ d_f \sin \theta_i + d_\theta \theta_i \cos \theta_i \end{bmatrix}, \quad (26)$$

$$\Delta\eta_i = \begin{bmatrix} d_f \cos \theta_i & -f_i d_\theta \sin \theta_i \\ d_f \sin \theta_i & f_i d_\theta \cos \theta_i \end{bmatrix}. \quad (27)$$

By substituting f_{\max} derived in (25) into (26) and (27), we can bound the perturbations as follows:

$$\|\Delta\eta\| \leq \max_{1 \leq i \leq n} \|\Delta\eta_i\|_F \leq \sqrt{d_f^2 + f_{\max}^2 d_\theta^2}, \quad (28)$$

$$\|\Delta\zeta\| = \sqrt{\sum_{i=1}^n \|\Delta\zeta_i\|^2} \leq \sqrt{n} f_{\max} \sqrt{d_f^2 + \theta_{\max}^2 d_\theta^2}. \quad (29)$$

\square

Theorem 2. Assume that $k_\mu > \frac{(1-\gamma)^2}{\gamma} \max\{\frac{M_1^2}{\lambda_{\min}(W_1)}, \frac{M_2^2}{\lambda_{\min}(W_2)}\}$ and $f_i > 0 \forall i$ with $\gamma = 1 - \|B\| \|\Delta\eta \eta^{-1}\| \|B^\dagger\| > 0$. Then, the error variable $x = [z_1; z_2; e_\mu]$ for the closed-loop system composed of (5), (6) and (14) with uncertain parameters in actuator time constant is bounded.

Proof. From (14), the proposed control input is specified using nominal values of α_f, α_θ as

$$u_c = \bar{\eta}^{-1} B^\dagger (\dot{\mu}_d - B\bar{\zeta} - k_\mu e_\mu - \kappa) \quad (30)$$

where $(\bar{\cdot})$ denotes the nominal counterpart using $\bar{\alpha}_f, \bar{\alpha}_\theta$. Substituting the proposed control law (30) into (19) yields

$$\begin{aligned} \dot{V} \leq & -k_\mu \left(1 - \|B\| \|\Delta\eta \eta^{-1}\| \|B^\dagger\|\right) \|e_\mu\|^2 + \|e_\mu\| \|B\| \|\Delta\zeta\| \\ & + \|B\| \|\Delta\eta \eta^{-1}\| \|B^\dagger\| \|\dot{\mu}_d - B\bar{\zeta} - \kappa\| \\ & - z_1^\top W_1 z_1 - z_2^\top W_2 z_2. \end{aligned} \quad (31)$$

Assume that the initial state x satisfies $V(x) \leq c$ for some positive constant c . By following a procedure similar to that used for (22), it follows that there exist positive constants M_0, M_1 , and M_2 such that

$$\|\dot{\mu}_d - B\bar{\zeta} - \kappa\| \leq M_0 + M_1 \|z_1\| + M_2 \|z_2\|. \quad (32)$$

Substituting (32) into (31) and applying Young's inequality, we obtain

$$\dot{V} \leq -\beta_1 \|e_\mu\|^2 - \beta_2 \|z_1\|^2 - \beta_3 \|z_2\|^2 + \beta_4 \quad (33)$$

where

$$\begin{aligned} \gamma &:= 1 - \|B\| \|\Delta\eta \eta^{-1}\| \|B^\dagger\| \\ \beta_1 &= \frac{1}{2} k_\mu \gamma, \beta_2 = \lambda_m(W_1) - \frac{(1-\gamma)^2 M_1^2}{k_\mu \gamma} \\ \beta_3 &= \lambda_m(W_2) - \frac{(1-\gamma)^2 M_2^2}{k_\mu \gamma}, \beta_4 = \frac{\|B\|^2 \|\Delta\zeta\|^2 + (1-\gamma)^2 M_0^2}{k_\mu \gamma}. \end{aligned}$$

Note that $\beta_2 > 0$ and $\beta_3 > 0$ by the assumption that $k_\mu > \frac{(1-\gamma)^2}{\gamma} \max\{\frac{M_1^2}{\lambda_{\min}(W_1)}, \frac{M_2^2}{\lambda_{\min}(W_2)}\}$.

At the equilibrium point, according to Lemma 1, V is quadratically lower bounded by x . Thus, from (33), there exists a positive constant c_v that satisfies $\dot{V} \leq -c_v V + \beta_4$, and this leads to boundedness of $\|x\|$ by comparison lemma [25]. \square

V. RESULTS

A. Experimental setup

We validate the proposed backstepping controller and evaluate its performance under uncertainty through hardware experiments. The tilttable quadrotor was equipped with Armattan 2450Kv rotors, APC $6 \times 4 \times 3.2$ propellers, and Dynamixel XC330-M288 servos. The flight controller utilized Pixhawk6C with PX4 software, and the on-board computer, ASUS NUC13, ran Robot Operating System 2 (ROS2) to directly control the actuators. For the odometry of the tiltrotor, we fused data from the indoor motion capture system, OptiTrack, and the IMU sensor data from the Pixhawk. The position and attitude controllers operated at 100 Hz and 200 Hz, respectively.

To generate the control inputs for the proposed backstepping controller, the total force and torque of the current state must be estimated. Additionally, to calculate the ζ matrix in (6), we estimated the thrusts f_i of each rotor and the state θ_i of the servos. Servomotors are typically equipped with encoders that provide direct angle feedback. The Dynamixel servos used in our system also include embedded encoders, which allow us to readily obtain estimates of the servo angles. In contrast, many ESCs for rotors do not report the rotor's angular velocity. To address this limitation, we estimated the rotor thrust indirectly. Specifically, we obtained wrench estimates by solving the inverse rigid-body dynamics using linear and angular acceleration estimates provided by PX4, following the approach of [22]. To mitigate high-frequency noise in the acceleration data from the sensors, we applied a low-pass filter with a cutoff frequency of 20 Hz to the estimated force and torque.

For all subsequent real-world experiments, we compare the proposed backstepping controller against a baseline framework consisting of a geometric PID motion controller [24] and a geometric allocation method [6] that does not account for actuator dynamics. The control gains were tuned during hovering at zero roll and pitch angles until sufficiently small translational and rotational errors were achieved. Under these conditions, the gains were further adjusted so that the baseline and the proposed method exhibited comparable performance levels.

To evaluate the performance of the proposed algorithm under aggressive maneuvers involving abrupt changes in control inputs, we designed three experimental scenarios. In the first and second experiments, we compared tracking performance during rapid translational and rotational motions, respectively. The third experiment involved recovering position and attitude under sudden external disturbance, which is also illustrated in Fig. 1. This disturbance was induced by suspending a 0.21 kg mass from a 2 kg drone with a string: the mass initially rested on a table, and as the drone moved laterally to the right, the mass applied an impulsive disturbance in the rotational direction.

B. Experiment 1

To evaluate agile position-tracking performance, we selected a lemniscate (figure-eight) trajectory. After takeoff, the vehicle maintained a constant altitude $z = 1.2$ m and tracked $x(t) = 0.4 \sin(\omega t)$, $y(t) = 0.3 \sin(2\omega t)$, while holding a fixed zero attitude. The average speed over one period was varied by adjusting the angular frequency ω to achieve 0.8, 1.0, and 1.2 m/s.

After the vehicle reached the target altitude and stabilized (5 s settling), we recorded data for five full cycles. In all three experiments with different average speeds, the proposed method successfully completed the tasks without losing stability, while the baseline diverged and lost stability during the final and fastest experiment at 1.2 m/s. The RMSE (Root Mean Square Error) of position and orientation errors for each experiment is summarized in Table I, which shows that the proposed method consistently achieved lower RMSE across

TABLE I
EXPERIMENT 1 RESULTS: POSITION AND ORIENTATION ERROR.
BETTER PERFORMANCE IN BOLD.

		Average Velocity		
		0.8 m/s	1.0 m/s	1.2 m/s
Proposed	pos. [m]	0.050	0.055	0.074
	rot. [rad]	0.057	0.077	0.132
Baseline	pos. [m]	0.070	0.072	×
	rot. [rad]	0.072	0.085	×

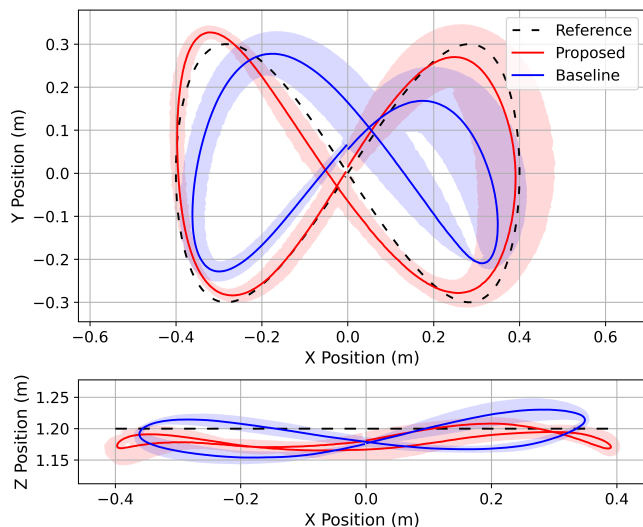


Fig. 3. Experiment 1 results. Three trials were conducted along a lemniscate (figure-eight) trajectory at different average speeds. The mean and variance are shown, excluding the failed baseline case at the highest speed where only the proposed method succeeded. Overall, the proposed method tracks the desired trajectory more accurately.

all scenarios. In Fig. 3, we visualize the results of the first two experiments, excluding the failed baseline case from the third experiment, using the mean values along with $\pm 1\sigma$ intervals. The variance is represented as translucent bands, while the mean values are plotted as solid lines. Additionally, at 200Hz we computed the position and rotation errors defined in Eq. (8) at every time step and report the component-wise RMSE averaged over all components in Table I.

C. Experiment 2

We further evaluate agile orientation-tracking performance by fixing the position and comparing the response under rapid roll oscillations. The desired roll angle was given as $\phi_d(t) = 50^\circ \sin(2\pi ft)$, and control performance was measured while varying the oscillation frequency $f \in \{0.4, 0.6, 0.8\}$ Hz.

In Fig. 4, along with the roll angle graphs, we also plot the lateral position component y that shows the largest deviation. The proposed controller yields noticeably smaller y -axis position errors than the baseline. As in Experiment 1, the position and rotational errors for each scenario are summarized in Table II. The proposed controller shows clearer superiority at higher frequencies, quantitatively supporting the

TABLE II
EXPERIMENT 2 RESULTS: POSITION AND ORIENTATION ERROR.
BETTER PERFORMANCE IN BOLD.

		Oscillation Frequency		
		0.4 Hz	0.6 Hz	0.8 Hz
Proposed	pos. [m]	0.042	0.037	0.050
	rot. [rad]	0.092	0.098	0.161
Baseline	pos. [m]	0.050	0.062	0.095
	rot. [rad]	0.113	0.133	0.284

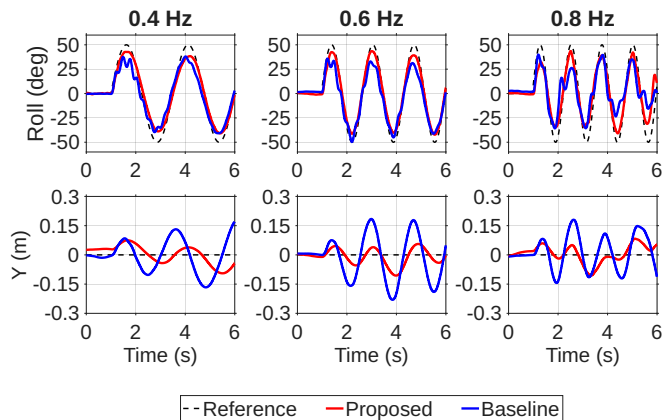


Fig. 4. Experiment 2 results. With position held fixed, the roll angle was rapidly varied. The proposed controller (red) achieved more accurate position regulation and orientation tracking than the baseline (blue).

expectation that it is well suited to agile reference trajectories that demand rapid rotor and servo state changes.

D. Experiment 3

Finally, to compare the baseline and proposed controllers under sudden changes in the desired inputs, we generated a repeatable, large impulsive external wrench. We connect the drone to a tabletop object by a lightweight tether with initial slack. The object's mass was 0.21 kg, approximately 10% of the drone's mass. As the drone translated away from the table, the object eventually dropped off the edge and the tether became taut, applying a short, high-magnitude disturbance to the drone (see Fig. 1). We evaluated each controller's capability to recover position and attitude.

For a fair comparison, all trials were conducted in the same environment with an identical reference trajectory. In each flight, the drone took off and then traveled 1 m along the x -axis at a constant speed. The recorded position and attitude are shown in Fig. 5. When the object falls, the roll angle suddenly reaches approximately -60° . The proposed controller stabilizes the vehicle and tracks the setpoint again, while the baseline becomes unstable and diverges.

VI. CONCLUSION

In this paper, we propose a geometric backstepping controller for an omnidirectional tiltrotor platform that integrates rotor and tilt-servo dynamics. Based on geometric PID control, we designed the controller within a backstepping

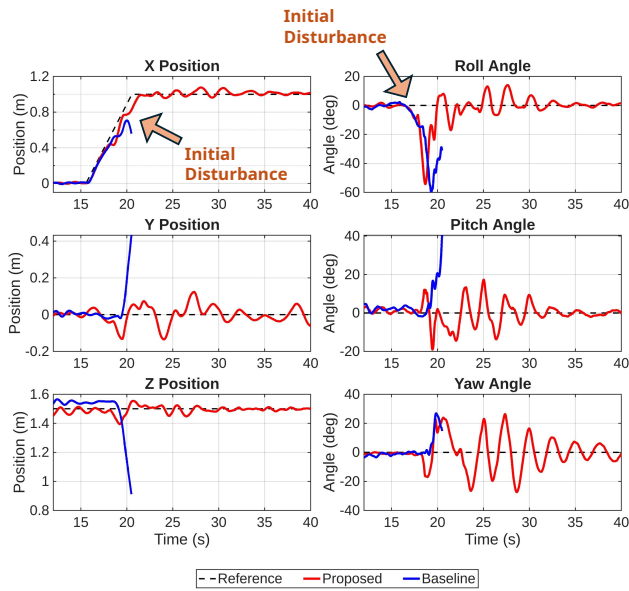


Fig. 5. Experiment 3 results. The initial disturbance, indicated by the yellow arrow, was caused when a 0.21 kg mass suspended by a string and initially resting on a table was pulled, applying a rotational disturbance to the multirotor. While the baseline diverged, the proposed controller stabilized the system and demonstrated superior performance.

framework and proved exponential stability under known actuator dynamics. Moreover, we confirmed through direct measurements that no single constant parameter can adequately represent the actuator time constants. To address this, we proved that the proposed controller ensures the boundedness of the closed-loop system even under bounded uncertainties of the actuator time constants. To validate the proposed controller on hardware, we conducted three experimental scenarios and compared it against a baseline geometric-allocation method. The controller demonstrated improved performance under rapid changes in control inputs. In particular, while the baseline often diverged and crashed, our method maintained stability in all cases. In future work, our aim is to strengthen the analysis to guarantee exponential stability under uncertainty and to evaluate the proposed controller across a wider range of tasks.

REFERENCES

- [1] R. Rashad, J. Goerres, R. Aarts, J. B. Engelen, and S. Stramigioli, "Fully actuated multirotor uavs: A literature review," *IEEE Robotics & Automation Magazine*, vol. 27, no. 3, pp. 97–107, 2020.
- [2] G. Park, H. Park, W. Park, D. Lee, M. Kim, and S. J. Lee, "The palletone cart: Human-robot interaction-based aerial cargo transportation," *IEEE Robotics and Automation Letters*, vol. 9, no. 8, pp. 6999–7006, 2024.
- [3] E. Cuniato, N. Lawrance, M. Tognon, and R. Siegwart, "Power-based safety layer for aerial vehicles in physical interaction using lyapunov exponents," *IEEE Robotics and Automation Letters*, vol. 7, no. 3, pp. 6774–6781, 2022.
- [4] G. He, X. Guo, L. Tang, Y. Zhang, M. Mousaei, J. Xu, J. Geng, S. Scherer, and G. Shi, "Flying hand: End-effector-centric framework for versatile aerial manipulation teleoperation and policy learning," *arXiv preprint arXiv:2504.10334*, 2025.
- [5] D. Brescianini and R. D'Andrea, "Design, modeling and control of an omni-directional aerial vehicle," in *2016 IEEE international conference on robotics and automation (ICRA)*. IEEE, 2016, pp. 3261–3266.

- [6] M. Kamel, S. Verling, O. Elkhatib, C. Sprecher, P. Wulkop, Z. Taylor, R. Siegwart, and I. Gilitschenski, "The voliro omniorientational hexacopter: An agile and maneuverable tiltable-rotor aerial vehicle," *IEEE Robotics & Automation Magazine*, vol. 25, no. 4, pp. 34–44, 2018.
- [7] M. Ryll, H. H. Bühlhoff, and P. R. Giordano, "A novel overactuated quadrotor unmanned aerial vehicle: Modeling, control, and experimental validation," *IEEE Transactions on Control Systems Technology*, vol. 23, no. 2, pp. 540–556, 2015.
- [8] K. Bodie, M. Brunner, M. Pantic, S. Walser, P. Pfändler, U. Angst, R. Siegwart, and J. Nieto, "Active interaction force control for contact-based inspection with a fully actuated aerial vehicle," *IEEE Transactions on Robotics*, vol. 37, no. 3, pp. 709–722, 2021.
- [9] D. Lee, B. Kim, and H. J. Kim, "Autonomous aerial manipulation at arbitrary pose in se (3) with robust control and whole-body planning," *arXiv preprint arXiv:2508.19608*, 2025.
- [10] D. Lee, S. Hwang, J. Byun, S. J. Lee, and H. J. Kim, "Autonomous aerial perching and unperching using omnidirectional tiltrotor and switching controller," in *2024 IEEE International Conference on Robotics and Automation (ICRA)*. IEEE, 2024, pp. 1590–1596.
- [11] J. Li, J. Sugihara, and M. Zhao, "Servo integrated nonlinear model predictive control for overactuated tilttable-quadrotors," *IEEE Robotics and Automation Letters*, 2024.
- [12] M. Allenspach, K. Bodie, M. Brunner, L. Rinsoz, Z. Taylor, M. Kamel, R. Siegwart, and J. Nieto, "Design and optimal control of a tiltrotor micro-aerial vehicle for efficient omnidirectional flight," *The International Journal of Robotics Research*, vol. 39, no. 10-11, pp. 1305–1325, 2020.
- [13] W. Park, X. Wu, D. Lee, and S. J. Lee, "Design, modeling and control of a top-loading fully-actuated cargo transportation multirotor," *IEEE Robotics and Automation Letters*, vol. 8, no. 9, pp. 5807–5814, 2023.
- [14] S. Seshasayanan, S. De, and S. R. Sahoo, "Robust attitude control with fixed exponential rate of convergence and consideration of motor dynamics for tilt quadrotor using quaternions," *IEEE Transactions on Automation Science and Engineering*, vol. 22, pp. 2445–2459, 2025.
- [15] J. S. Bang, H. Shim, S. K. Park, and J. H. Seo, "Robust tracking and vibration suppression for a two-inertia system by combining backstepping approach with disturbance observer," *IEEE transactions on industrial electronics*, vol. 57, no. 9, pp. 3197–3206, 2009.
- [16] E. Cuniato, M. Allenspach, T. Stastny, H. Oleynikova, R. Siegwart, and M. Pantic, "Allocation for omnidirectional aerial robots: Incorporating power dynamics," *arXiv preprint arXiv:2412.16107*, 2024.
- [17] S. Bouabdallah and R. Siegwart, "Backstepping and sliding-mode techniques applied to an indoor micro quadrotor," in *Proceedings of the 2005 IEEE international conference on robotics and automation*. IEEE, 2005, pp. 2247–2252.
- [18] T. Lee, M. Leok, and N. H. McClamroch, "Geometric tracking control of a quadrotor uav on se (3)," in *49th IEEE conference on decision and control (CDC)*. IEEE, 2010, pp. 5420–5425.
- [19] M. Faessler, D. Falanga, and D. Scaramuzza, "Thrust mixing, saturation, and body-rate control for accurate aggressive quadrotor flight," *IEEE Robotics and Automation Letters*, vol. 2, no. 2, pp. 476–482, 2016.
- [20] E. Tal and S. Karaman, "Accurate tracking of aggressive quadrotor trajectories using incremental nonlinear dynamic inversion and differential flatness," *IEEE Transactions on Control Systems Technology*, vol. 29, no. 3, pp. 1203–1218, 2020.
- [21] D. Brescianini and R. D'Andrea, "An omni-directional multirotor vehicle," *Mechatronics*, vol. 55, pp. 76–93, 11 2018.
- [22] H. Lee, S. Cheng, Z. Wu, J. Lim, R. Siegwart, and N. Hovakimyan, "Geometric tracking control of omnidirectional multirotors for aggressive maneuvers," *IEEE Robotics and Automation Letters*, 2025.
- [23] H. Lee, B. Yu, C. Tirtawardhana, C. Kim, M. Jeong, S. Hu, and H. Myung, "CAROS-Q: Climbing aerial robot system adopting rotor offset with a quasi-decoupling controller," *IEEE Robotics and Automation Letters*, vol. 6, no. 4, pp. 8490–8497, 2021.
- [24] F. Goodarzi, D. Lee, and T. Lee, "Geometric nonlinear pid control of a quadrotor uav on se (3)," *arXiv preprint arXiv:1304.6765*, 2013.
- [25] H. K. Khalil and J. W. Grizzle, *Nonlinear systems*. Prentice hall Upper Saddle River, NJ, 2002, vol. 3.